JOURNAL OF AIRCRAFT
Vol. 43, No. 4, July–August 2006

Rolling Moment Characteristics of Supersonic Transport Configuration at High-Incidence Angles

Dong-Youn Kwak* and Masayoshi Noguchi†
Japan Aerospace Exploration Agency, Tokyo 181-0015, Japan
and
Masashi Shirotake‡ and Kenichi Rinoie§
University of Tokyo, Tokyo 113-8656, Japan

Wind-tunnel tests were performed to investigate rolling moment characteristics of a cranked arrow wing supersonic transport configuration at high incidence angles. Force measurements and surface static pressure measurements were conducted when the wing model was rolled statically at a Reynolds number of 9.21×10^3 based on the mean aerodynamic chord. To understand the behavior of the leading-edge separation vortices formed both on the inboard and outboard of the cranked arrow wing, a stereoscopic particle image velocimetry survey was performed at 55 and 83% root chord locations. As the wing roll angle was increased, linear stable rolling moments were observed at low incidence angles, whereas abrupt changes from stable to unstable rolling moments were observed at incidence angle of 20 deg. Variations in suction peaks of pressure distributions at the rear part of the wing contribute to destabilization of the rolling moment component. These variations in suction peaks that induce the unstable rolling moment are related to the vortex breakdown characteristics. Chordwise breakdown locations of the inboard and outboard vortices are different between the windward and leeward wings. This difference causes the sudden change of rolling moments.

Nomenclature

b = local semispan length, m
$b_{\max}$ = wing maximum semispan length, m
C_m = pitching moment coefficient referred to body axis nondimensionalized using c_{mac} and measured about 0.25 c_{mac} (nose-up direction positive)
C_p = pressure coefficient
C_{rol} = rolling moment coefficient referred to body axis nondimensionalized using full span length
c_{mac} = wing mean aerodynamic chord length, m
c_r = wing root chord length at model centerline, m
Re = Reynolds number based on mean aerodynamic chord
U = freestream velocity, m/s
u = x-direction flow velocity of body axis, m/s
v = y-direction flow velocity of body axis, m/s
w = z-direction flow velocity of body axis, m/s
x = chordwise coordinate measured from apex of cranked arrow wing at model centerline, m
y = spanwise coordinate measured orthogonal to x from model centerline, m
z = vertical coordinate measured orthogonal to x from model centerline, m
α = angle of attack, deg
β = side-slip angle, deg
Λ = sweepback angle, deg
Λ_{eff} = effective sweepback angle, deg
σ = incidence angle (angle that is composed of direction of freestream and x-direction of body axis), deg
ϕ = roll angle (clockwise direction is positive on rear view), deg

Presented as Paper 2003-3413 at the AIAA 21st Applied Aerodynamic Conference, Orlando, FL, 23–27 June 2003; received 30 May 2005; revision received 13 November 2005; accepted for publication 14 November 2005. Copyright © 2006 by the American Institute of Aeronautics and Astronautics, Inc. All rights reserved. Copies of this paper may be made for personal or internal use, on condition that the copier pay the $10.00 per-copy fee to the Copyright Clearance Center, Inc., 222 Rosewood Drive, Danvers, MA 01923; include the code 0021-8669/06 $10.00 in correspondence with the CCC.

*Senior Researcher, Advanced Aircraft Technology Center, 6-13-1 Osawa, Mitaka. Member AIAA.
†Senior Researcher, Advanced Aircraft Technology Center, 6-13-1 Osawa, Mitaka.
‡Graduated Student, Department of Aeronautics and Astronautics, 7-3-1 Hongo, Bunkyo-ku.
§Professor, Department of Aeronautics and Astronautics, 7-3-1 Hongo, Bunkyo-ku. Senior Member AIAA.

I. Introduction

A SUPERSONIC transport (SST) configuration has a higher sweepback angle and lower aspect ratio wing, such as a delta wing or a cranked arrow wing. At high-angle-of-attack flight, such as takeoff and landing, flow separates from the leading edges of the wing, rolls up on the upper surface, and forms leading-edge separation vortices over the wing. Because leading-edge separation vortices induce nonlinear suction force (often referred to as vortex lift), the aerodynamic characteristics of the SST configuration are strongly influenced by the vortex behavior.[1]

The vortex behavior formed on the delta wing configurations has been studied for the past several decades.[2–8] The strength of the leading-edge separation vortex on the delta wing is strongly influenced by wing angles of attack and sweepback angles. At relatively low angles of attack, smooth changes of the aerodynamic forces are observed because the strength of the vortex changes almost continually as the wing attitude is changed. However, nonlinear aerodynamic phenomena such as 1) a vortex breakdown[9,10] and 2) a vortex liftoff[11,12] are observed in the behavior of the leading-edge separation vortex at high angles of attack. The vortex breakdown is a well-known phenomenon that induces a loss of vortex lift. The vortex liftoff is a phenomenon that occurs when the leading-edge separation vortex moves away from the wing surface, causing a drastic reduction in the vortex lift. Similar flow phenomena are observed for an ogive–cylinder at high angles of attack.[13]

When the wing is rolled, the vortex behavior is different for the windward and leeward wings. This asymmetric vortex behavior affects the roll characteristics. At high angle of attack, the nonlinear aerodynamic phenomena mentioned also occur asymmetrically on the windward and leeward wings. Therefore, this vortex behavior induces abrupt and complex changes in the rolling moment characteristics.[5,6] As for a double delta wing and a cranked arrow wing, two pairs of leading-edge separation vortices are formed, both

from the inboard and outboard leading edges of these wings; these have different leading-edge sweepback angles. These inboard and outboard vortices interact with each other[14,15] and strongly affect vortex behavior. Therefore, the roll characteristics of the double delta and the cranked arrow wing configurations are assumed to be more complex than the delta wing configurations.

In this study, rolling moment characteristics of a cranked arrow wing SST configuration at high incidence angles were investigated in a low-speed wind tunnel. Force and surface pressure measurements were performed to understand the roll characteristics of the cranked arrow wing. Stereoscopic particle image velocimetry (PIV) measurements were also conducted to analyze the behavior of the inboard and outboard leading-edge separation vortices formed on the wing.

II. Experimental Details

Figure 1 shows an SST model that was preliminarily designed by the supersonic transport program of the Japan Aerospace Exploration Agency (JAXA).[16] This SST configuration model consists of a cranked arrow wing and a fuselage. A kink is located at $y/b_{\max} = 0.55$ that connects the inboard wing of 66-deg sweepback angle and the outboard wing of 42-deg sweepback angle. The wing has a warped wing section designed by the supersonic lifting surface theory to optimize the twist and camber distributions at a design Mach number of 1.7 (Ref. 16). The SST model has static pressure tappings on the upper surface of the left wing at $x/c_r = 0.55$ and 0.83, as shown in Fig. 1. The inboard wing has the thickness distribution of a NACA66-series airfoil section with an average thickness chord ratio of 3%. The outboard wing has a biconvex airfoil section with a maximum thickness chord ratio of 3%. Further details of the wing cross section are described in Ref. 17.

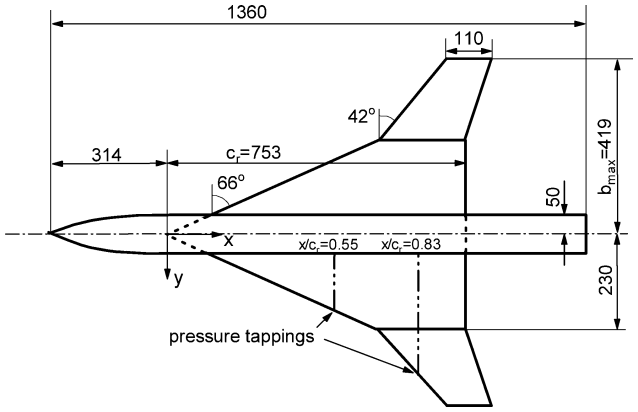

Fig. 1 Schematic of cranked arrow SST configuration, millimeters.

The experiments were conducted in a 2×2 m low-speed wind tunnel at JAXA. The freestream velocity was $U = 30$ m/s and the Reynolds number based on the mean aerodynamic chord was $Re = 9.21 \times 10^5$. A schematic of the wind-tunnel tests is shown in Fig. 2. The SST model was supported by an industrial multipurpose robot arm via a sting. The robot arm can control the model attitude with six degrees of freedom within 0.5-mm accuracy. In the present test, the model was rotated to a roll direction at a fixed incidence angle σ. The tested incidence angles were 12, 16, 18, and 20 deg. The tested roll angles ϕ were in a range from -30 to 30 deg.

Aerodynamic forces were measured by means of a six-component internal balance. The definition of the rolling moment is based on the body axis. Electronic scanning pressure sensors were used to measure the surface static pressure distributions. We checked that the flow settled down to a steady state whenever the model was set to a new roll angle and then averaged the force data obtained from the internal balance by sampling 500 times with 2-ms intervals. Force data were obtained by rolling the model at 2.5-deg increments from $\phi = -30$ to 30 deg and by rolling back from $\phi = 30$ to -30 deg, which comprises one cycle of the measurements. Pressure data were obtained by averaging 100 sampled data recorded at 5-ms intervals. The estimated overall uncertainties of the rolling moment coefficients C_{rol} and the pressure coefficient C_P are less than ± 0.5 and $\pm 2\%$ at 20:1 odds. Force measurements and pressure measurements were conducted separately to avoid any disturbance to the internal balance from the pressure tubing.

Stereoscopic PIV surveys were performed to understand the overall behavior of flow at $x/c_r = 0.55$ and 0.83 on the upper surface. The PIV system (Fig. 2) mainly consists of 200-mJ double-pulse Nd:YAG lasers to illuminate the seeding particles in the flow, two charge-coupled device (CCD) cameras with 1280×1024 pixels to acquire images of the illuminated particles, and a personal computer to control the equipment and to conduct data processing. Detailed information on the present PIV system is described in Ref. 18. Oil droplets of an approximate average diameter of 1 μm were inserted into the flow as seeding particles. The laser light sheet, introduced through an upper optical window of the test section, illuminates the seeding particles over the upper surface of the model, which is parallel to the y–z plane based on the model body axis. Two CCD cameras were located at the port side of the test section. Each camera acquired instantaneous two laser sheets of particle images at 30-μs time intervals. Three component velocities, u, v, and w, were calculated from images captured by the two CCD cameras. The typical imaging area size was 200 mm in width and 80 mm in height, where 98×40 velocity vectors are measured in this area. When these measured velocity vectors were plotted, the number of velocity vectors was reduced for easy of viewing. The averaged flow velocity vector distributions were obtained by averaging 300–900 sheets of instantaneous velocity vector images with an acquisition rate of 2 Hz.

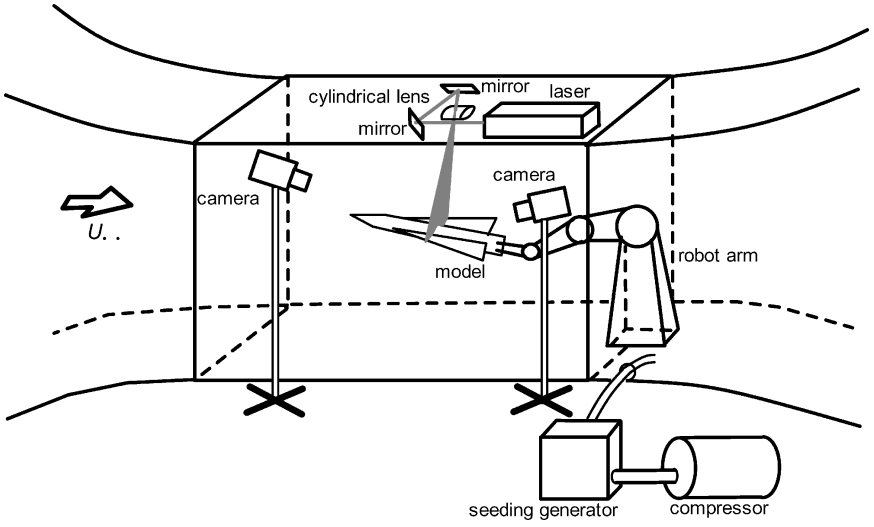

Fig. 2 Schematic of PIV setup (seen from port side).

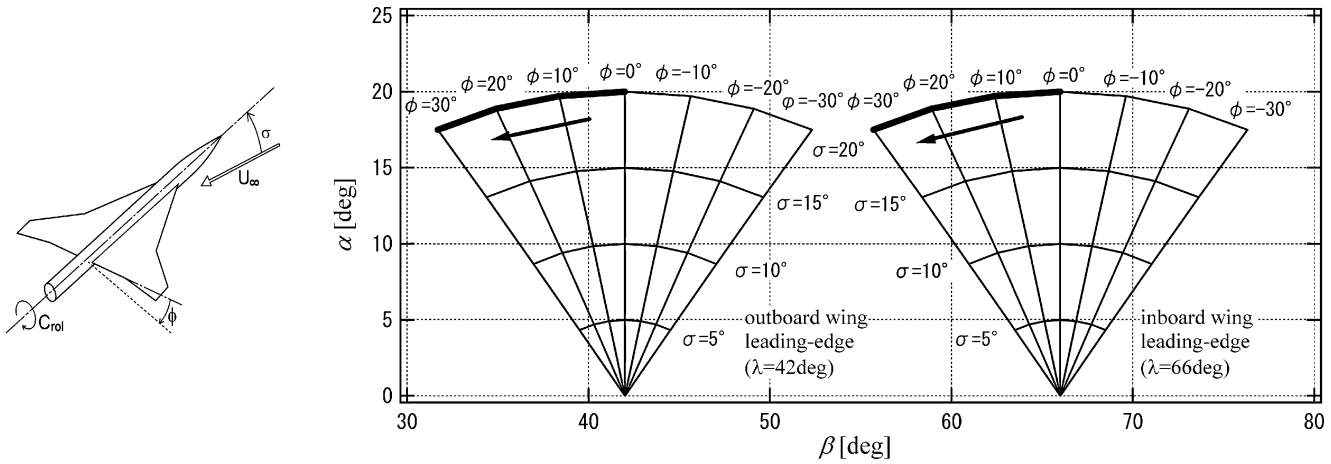

Fig. 3 Variation of angle of attack and effective sweepback angle on inboard and outboard leading edge of right wing.

The estimated overall uncertainty of the averaged velocity by PIV measurements is less than ±10% at 20:1 odds.

III. Geometric Relations of Wing Attitude

Figure 3 shows variations in angle of attack and effective sweepback angle on the inboard and outboard leading edges for the right wing when the wing model is rotated to a roll direction at a fixed incidence angle. For example, when a roll angle changes from 0 to 30 deg (positive roll direction) at the incidence angle σ fixed to 20 deg (bold line in Fig. 3), the angle of attack α decreases from 20 to 17.5 deg. The same results are obtained when the model is rotated to a negative roll direction. This means that when the model is rotated to an arbitrary roll angle, $\phi_1 \neq 0$ deg, although the incidence angle is fixed, the angles of attack on the windward and leeward wings are the same, and they are smaller than the incidence angle. However, the effective sweepback angle Λ_{eff} on the leading edge of the windward and leeward wings is different. The effective sweepback angle on the windward wing is smaller than Λ, and Λ_{eff} on the leeward wing is larger than Λ. This asymmetry of the effective sweepback angle of the windward and leeward wings induces the asymmetric behavior of the leading-edge vortices.

IV. Results and Discussion

A. Rolling Moment Characteristics

Figure 4 shows the static rolling moment characteristics at several incidence angles of σ. Linear and stable (restoring) rolling moment coefficients C_{rol} are observed at low incidence angles, $\sigma = 12$ and 16 deg. At $\sigma = 20$ deg, linear and stable rolling moments are observed at small roll angles, $|\phi| \leq 10$ deg, whereas the C_{rol} changes drastically from a stable state to an unstable one at $|\phi| = 15$–25 deg. When ϕ is increased up to 30 deg, the absolute value of C_{rol} decreases, but it still maintains an unstable state.

Figure 5 shows the pitching moment coefficients C_m when the model has roll angles, as shown in Fig. 4. At incidence angles of $\sigma = 12$ and 16 deg, nose-down pitching moments decrease slightly as roll angles increase from $\phi = 0$ to 30 deg. An abrupt change in the nose-down pitching moment is observed near $\phi = 15$–25 deg at $\sigma = 20$ deg. These roll angles of $\phi = 15$–25 deg correspond to those when a drastic change in the rolling moment was observed, as in Fig. 4.

As mentioned in the preceding section, the effective sweepback angle Λ_{eff} on the windward wing is smaller than that of the leeward wing. In Ref. 19, it is discussed how higher suction force is induced on the delta wing with a smaller sweepback angle. This discussion on the induced suction force can also be applied to the present results. Higher suction force acts on the windward wing producing a restored rolling moment, as was observed when $\sigma = 12$ and 16 deg (Fig. 4).

Ericsson and Hanff[20] reported that vortex breakdown induces the C_{rol} instability of the delta wing. The present results indicate that

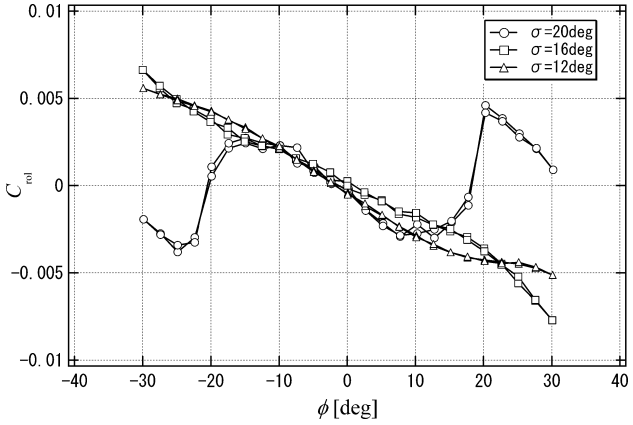

Fig. 4 Rolling moment characteristics at different incidence angles.

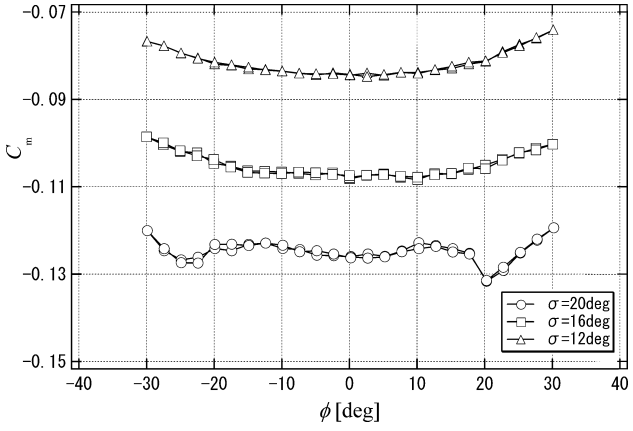

Fig. 5 Pitching moment characteristics at different incidence angles.

the C_{rol} instability is observed for the cranked arrow wing configuration at the high incidence angle of $\sigma = 20$ deg and suggest that the instability of C_{rol} is induced by vortex breakdown. Further details will be discussed in the following sections.

Figures 4 and 5 contain two curves with the same symbol at the same σ, for example, curves for $\sigma = 20$ deg. As explained in Sec. II, force data were obtained by rolling the model from $\phi = -30$ to 30 deg (clockwise direction seen from downstream of the model) and by rolling back from $\phi = 30$ to -30 deg (counterclockwise direction). It has been reported that the vortex breakdown on the delta wing often induces a large-scale flow hysteresis in the force and moment measurements, that is, a different force or moment

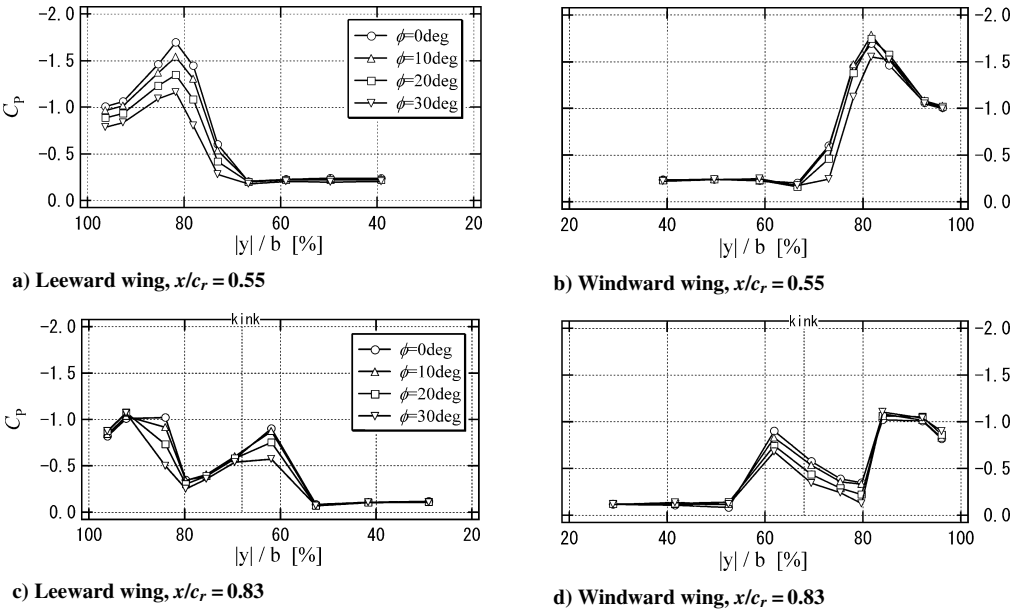

a) Leeward wing, $x/c_r = 0.55$

b) Windward wing, $x/c_r = 0.55$

c) Leeward wing, $x/c_r = 0.83$

d) Windward wing, $x/c_r = 0.83$

Fig. 6 Pressure distributions at different roll angles, $\sigma = 12$ deg.

is measured when the model is rolled in the clockwise direction and in the counterclockwise direction.[5,6,11] To check whether the flow hysteresis is observed in the present SST configuration, both results when the model is rotated in the clockwise direction and in the counterclockwise direction are plotted independently. It is seen that two curves almost coincide each other at the same incidence angle in Figs. 4 and 5, and no obvious difference is observed. These results suggest that the large-scale flow hysteresis does not occur within the present tested range. On the other hand, small differences between the two curves with the same symbol are observed at the same σ, for example, symbols at $\phi = 20$ deg and $\sigma = 20$ deg. These small differences between the two curves are more easily observed at $\sigma = 20$ deg than at $\sigma = 12$ and 16 deg. It is suggested that the unsteady flow and the critical states[21] at high alpha aerodynamics cause these small differences on the force and moment curves.

B. Static Pressure Distributions

Static pressure tappings were installed on the left wing of the SST model (Fig. 1). No data of static pressure on the right wing were measured. Therefore, to expand the analysis of measured static pressure distributions C_p on the left wing, an assumption was made as follows: Similar flows are realized both on the right wing when the model has an positive roll angle, $\phi_p > 0$ deg, and on the left wing when the model has a negative roll angle, $\phi_n = -\phi_p$. For example, C_p distributions on the left wing at $\phi = -20$ deg correspond to those on the right wing at $\phi = 20$ deg. This assumption makes it possible to obtain rolling moment components from the upper surface C_p distributions. Arena and Nelson[22] and Chaderjian[23] measured and numerically analyzed the C_p distributions on the lower surface of delta wings with 80- and 65-deg sweepback angles. From these results, it was suggested that the C_p distributions on the lower surface of the delta wing do not change obviously when the wings are rotated to the roll direction. It is thought that the lower surface C_p distributions of the present SST configuration behave similarly to these delta wings. Therefore, it can be said the essential rolling moment characteristics can be understood without lower surface C_p distributions. The effect of spanwise local contribution of C_p on the roll stability will be discussed.

Figure 6 shows C_p distributions at $x/c_r = 0.55$ and 0.83 when $\sigma = 12$ deg and $\phi = 0$–30 deg. C_p distributions on the right wing (windward wing) when $\phi > 0$ deg (Figs. 6b and 6d) are plotted using this assumption. A suction peak is observed in the C_p distributions at $x/c_r = 0.55$ (Figs. 6a or 6b) that is induced by an inboard leading-edge separation vortex. Two suction peaks that are observed at $x/c_r = 0.83$ (Figs. 6c or 6d) are induced by the inboard and outboard leading-edge separation vortices. Variations in suction peaks at different roll angles can be attributed to the behavior of the leading-edge separation vortices. At $\sigma = 12$ deg the C_p distributions on the leeward wing at $x/c_r = 0.55$ and 0.83 (left wing, Figs. 6a and 6c) indicate that the suction peaks decrease as the roll angle increases, whereas the suction peaks on the windward wing at $x/c_r = 0.55$ and 0.83 (right wing, Figs. 6b and 6d) decrease only slightly. Both angle of attack α and effective sweepback angle Λ_{eff} on the windward wing decrease with increasing roll angle. On the other hand, α decreases and Λ_{eff} increases on the leeward wing (Fig. 3). On the windward wing, a decrease in α induces a decrease in the C_p suction, and a decrease in Λ_{eff} induces an increase in the C_p suction.[20] These α and Λ_{eff} geometric effects on the change in the C_p distributions cancel each other out. Thus, the C_p suction of the windward wing shown in Figs. 6b and 6d was not changed obviously. On the other hand, a decrease in α and an increase in Λ_{eff} on the leeward wing induced a decrease in C_p suction, as observed in Figs. 6a and 6c.

Figure 7 shows C_p distributions at $\sigma = 20$ deg. When compared with the results at $\sigma = 12$ deg in Fig. 6, similar trends can be seen for all cases at $x/c_r = 0.55$, but are different at $x/c_r = 0.83$. Figures 7c and 7d indicate that the inner and outer suction peaks on the windward wing decrease with increasing roll angle, and the inner suction peak on the leeward wing increases significantly with increasing roll angle up to 20 deg. These flowfields at $\sigma = 20$ deg and at $x/c_r = 0.83$ were visualized by means of the PIV technique and will be discussed in the next section.

Next, we discuss spanwise distributions of local rolling moment components that can be obtained both from upper surface C_p distributions on the right wing $C_{p\,\text{right}}$ and from those on the left wing $C_{p\,\text{left}}$ at each chordwise station. Figure 8 shows $\Delta C_p|y|$ distributions, where

$$\Delta C_p|y| = (C_{p\,\text{right wing}} - C_{p\,\text{left wing}}) \times |y| \tag{1}$$

The actual local rolling moment caused by the flow on the upper surface at a specific chordwise location is obtained by integrating the $\Delta C_p|y|$ in a spanwise direction. When this integrated value of $\Delta C_p|y|$ is negative, the negative closed area that is composed of a $\Delta C_p|y|$ curve and the $\Delta C_p|y| = 0$ axis contributes to the stabilization of the rolling moment by acting on the wing. On the other hand, when it is positive, the positive closed area contributes to the destabilization of the rolling moment. The magnitude of the area indicates the strength of roll stability. Therefore, contributions to

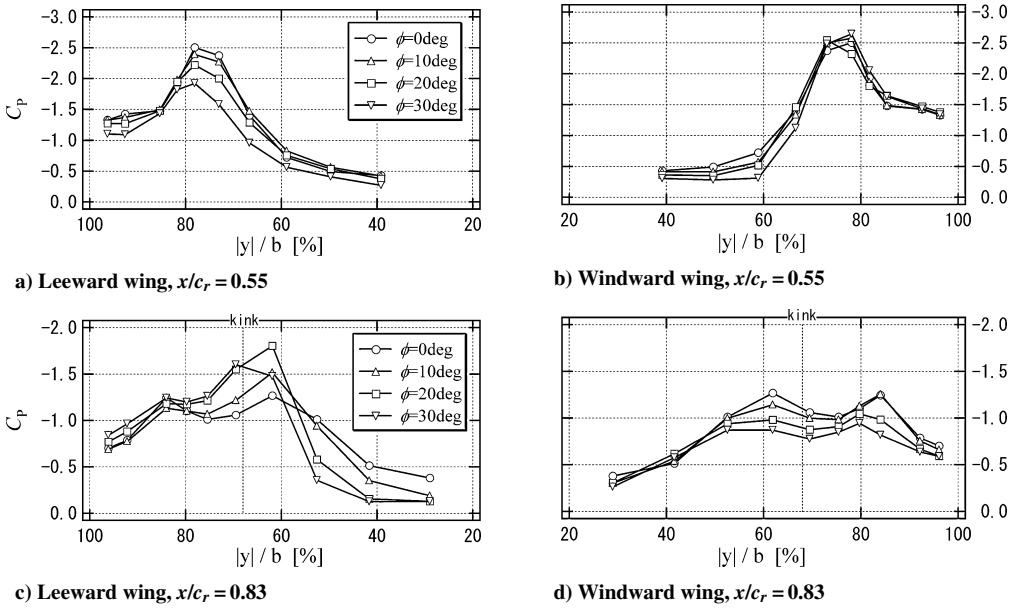

a) Leeward wing, $x/c_r = 0.55$

b) Windward wing, $x/c_r = 0.55$

c) Leeward wing, $x/c_r = 0.83$

d) Windward wing, $x/c_r = 0.83$

Fig. 7 Pressure distributions at different roll angles, $\sigma = 20$ deg.

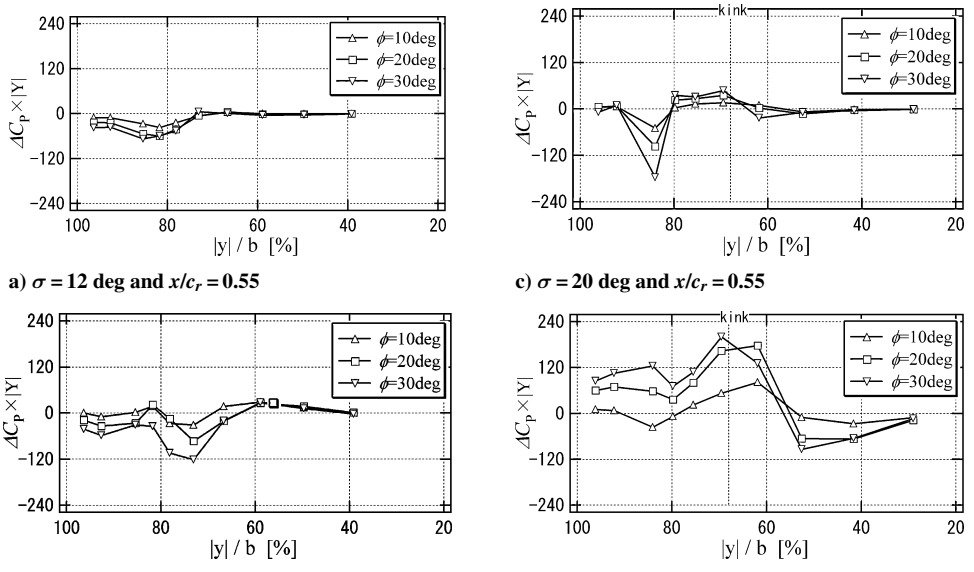

a) $\sigma = 12$ deg and $x/c_r = 0.55$

c) $\sigma = 20$ deg and $x/c_r = 0.55$

b) $\sigma = 12$ deg and $x/c_r = 0.83$

d) $\sigma = 20$ deg and $x/c_r = 0.83$

Fig. 8 Distributions of local rolling moment components at different roll angles.

the roll stability can be understood from Fig. 8. Figures 8a and 8c indicate that the $\Delta C_p|y|$ distribution at $x/c_r = 0.55$ is negative at spanwise locations where the inboard vortex is formed at $\sigma = 12$ and 20 deg. This means that the inboard vortex on the upper surface at $x/c_r = 0.55$ contributes to the stabilization of the rolling moment components. Figure 8b at $x/c_r = 0.83$ and $\sigma = 12$ deg indicates large negative $\Delta C_p|y|$ near the outer suction peak at about $y/b = 0.85$. However, in Fig. 8d, positive values of the $\Delta C_p|y|$ are observed near the inner and outer suction peaks at $x/c_r = 0.83$ and $\sigma = 20$ deg. These positive values at $\sigma = 20$ deg contribute to the destabilization of the rolling moment components.

Figure 9 shows local rolling moments of different incidence angles at $x/c_r = 0.55$ and 0.83. They were obtained by integrating the $\Delta C_p|y|$ distributions from the body centerline to the leading edges in a spanwise direction. Stable, that is, negative, local rolling moments at $x/c_r = 0.55$ (Fig. 9a) are observed at $\sigma = 12$–18 deg. They decrease linearly as the roll angle is increased up to $\phi = 30$ deg. At $x/c_r = 0.83$ (Fig. 9b), local rolling moments are negative at $\sigma = 12$ and 16 deg, which means that the stable rolling moment is acting on the wing. However, the unstable (positive) moment is observed at $\sigma = 18$ and 20 deg. Furthermore, nonlinear behavior of the local rolling moment is observed at $\sigma = 20$ deg. Although the local rolling moment at $\sigma = 20$ deg is stable at $\phi = 5$ deg, the unstable moment is observed up to $\sigma = 25$ deg. The further increase in the roll angle and magnitude of the unstable local rolling moment decreased at $\phi = 30$ deg. This local rolling moment at $x/c_r = 0.83$ does not exactly represent the rolling moment acting on the wing because the whole wing surface must be considered to estimate the rolling moment. However, the distribution pattern of the local rolling moment at $x/c_r = 0.83$ and $\sigma = 20$ deg in Fig. 9b is relatively similar to those of C_{rol} when $\phi > 0$ deg in Fig. 4. Therefore, it is thought that some of the rolling moment characteristics can be explained by the use of this local rolling moment concept, and it can be said that the nonlinear behavior of the local rolling moment at $x/c_r = 0.83$ and $\sigma = 20$ deg has a strong relationship with the abrupt change of rolling moment observed at $\sigma = 20$ deg in Fig. 4.

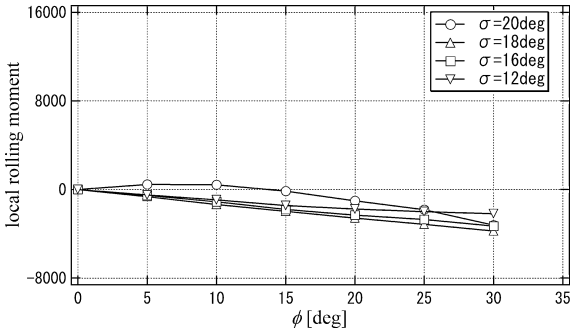

a) $x/c_r = 0.55$

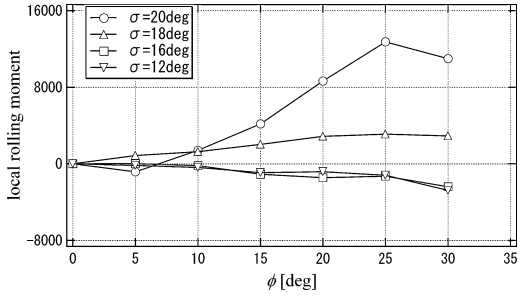

b) $x/c_r = 0.83$

Fig. 9 Local rolling moments in different incidence angles obtained from integration of $\Delta C_p|y|$ distributions.

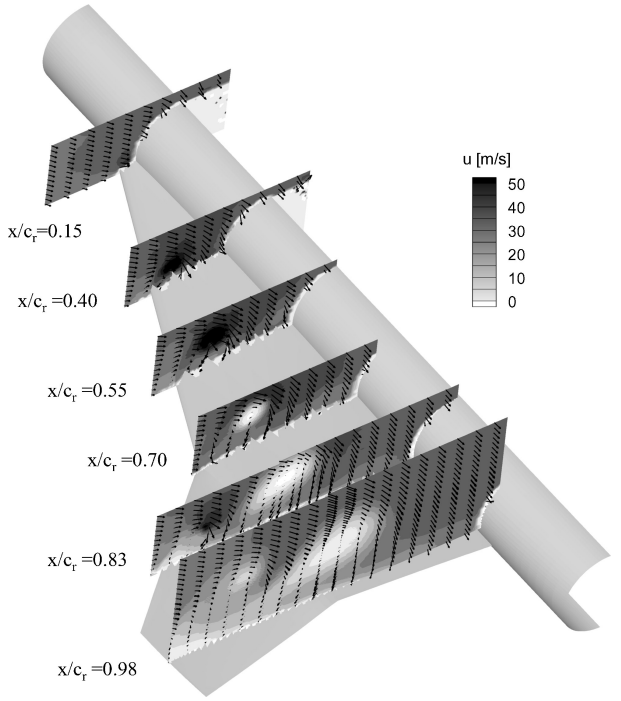

Fig. 10 Averaged velocity vectors and streamwise velocity contour at several chordwise locations, $\sigma = 20$ deg and $\sigma = 0$ deg.

From these results, it can be explained that C_p distributions at $x/c_r = 0.55$ at tested incidence angles contribute to the stabilization of the rolling moment components. At $x/c_r = 0.83$, C_p distributions at low incidence angles contribute to roll stabilization, whereas those at high incidence angles contribute to roll destabilization.

C. PIV Survey

To understand the overall flowfields at $\sigma = 20$ deg and $\phi = 0$ deg, average velocities were measured by PIV. The total velocity vector, $[u^2 + v^2 + w^2]^{1/2}$, and the u-velocity contour are plotted on the plane normal to the body axis at different chordwise locations in Fig. 10. The inboard and outboard leading-edge separation vortices are clearly observed in Fig. 10. Spanwise locations of inboard and outboard vortex centers at $x/c_r = 0.55$ and 0.83 almost coincide with the locations of the suction peaks in the C_p distributions (Fig. 7). These results reconfirm that leading-edge separation vortices induce high suction peaks in the C_p distributions. For the inboard vortex in Fig. 10, abrupt decrease in the streamwise velocity is observed downstream of $x/c_r = 0.70$, which is thought to be caused by vortex breakdown. When vortex breakdown occurs, the vorticity in the vortex is lost and the maginitude of the velocity parallel to the vortex axis drastically decreases.[7] Here, we consider that vortex breakdown has occurred when the x-direction velocity u is suddenly lost and is nearly 0 m/s. Note in Fig. 10 that vortex breakdown of the inboard vortex occurs upstream of $x/c_r = 0.83$. This corresponds to an indistinct suction peak of C_p observed near $|y|/b = 0.6$ at $\sigma = 20$ deg and $x/c_r = 0.83$ when $\phi = 0$ deg in Fig. 7c. In Fig. 10, the concentrated outboard vortex is formed near the wing surface at $x/c_r = 0.83$. However, this outboard vortex has been lifted off from the wing surface at $x/c_r = 0.98$ when compared with the one at $x/c_r = 0.83$. This liftoff is caused by the interaction between the inboard and outboard vortices.[14]

Figures 11 and 12 show average velocity vectors and streamwise velocity contours at $x/c_r = 0.83$ for different roll angles at $\sigma = 12$ deg (Fig. 11) and at $\sigma = 20$ deg (Fig. 12). To clarify the behavior of inboard and outboard vortices, the required whole imaging area (about 250×80 mm) covering the inboard and outboard vortices on the left and right wing was horizontally divided into two frames with some overlapping area when the PIV measurements were conducted at $\sigma = 20$ deg. In Figs. 11b and 12b, the velocity distributions on the leeward wing at $\phi = 20$ deg could not be obtained because the model fuselage interrupted the view angle from the CCD cameras.

Figure 11 indicates that as the roll angle is increased up to $\phi = 20$ deg at the fixed incidence angle of $\sigma = 12$ deg, the streamwise velocity u in the inboard vortex on the windward wing (right wing) slightly decreases. This behavior of the inboard wing makes the C_p suction peak on the windward wing decrease slightly, as was shown in Fig. 6d. At $\sigma = 20$ deg (Fig. 12), an area where u is nearly 0 m/s is observed at the center area of the inboard vortex on the windward wing, which indicates the onset of vortex breakdown. Similar behavior in the inboard vortex was already observed at $x/c_r = 0.70$, 0.83, and 0.98 in Fig. 10. Figure 12 also indicates the enlargement of the area where u is nearly 0 m/s on the windward wing as the roll angle is increased. On the other hand, shrinking of the area where u is nearly 0 m/s in the inboard vortex on the leeward wing is observed as the roll angle is increased because a concentrated vortex is reconstructed due to the retreat of vortex breakdown. This inboard vortex behavior at $x/c_r = 0.83$ can be explained by the characteristic vortex breakdown of the delta wings.[19] As the roll angle is increased, the chordwise location of vortex breakdown on the windward wing moves toward the wing apex. The chordwise location of the breakdown onset on the leeward wing retreats toward the trailing edge. These asymmetric chordwise movements of the vortex breakdown location on the windward and leeward wings induce unstable rolling moment components for the delta wing. The same tendency is observed in Fig. 12 for the inboard vortex of the present cranked arrow wing configuration. The asymmetric behavior of vortex breakdown of the inboard vortex induces asymmetric change in the suction peaks of C_p, which contributes to the destabilization of the rolling moment components. Furthermore, when the model is rolled from $\phi = 10$ to 20 deg, obvious reduction in the u velocity at the center of the outboard vortex on the windward wing is observed as shown in Fig. 12. This corresponds to the decrease in the suction peak that was shown in Fig. 7d. This behavior of the outboard vortex also induces the unstable rolling moment components. The varying behavior between the inboard and outboard vortices contributes to the abrupt change of rolling moments from a stable to an unstable state at $\sigma = 20$ deg, as was shown in Fig. 4.

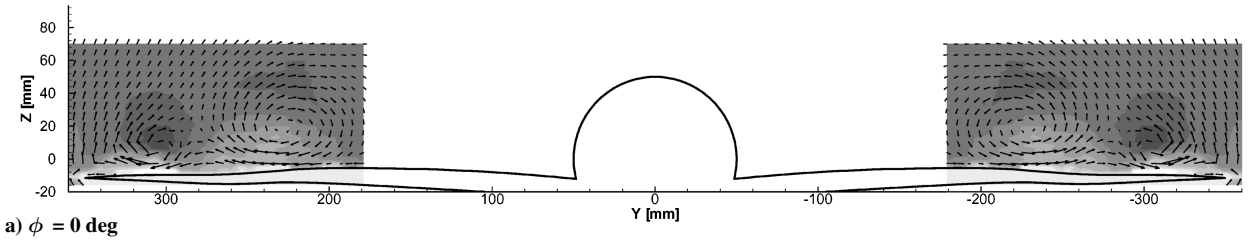

a) ϕ = 0 deg

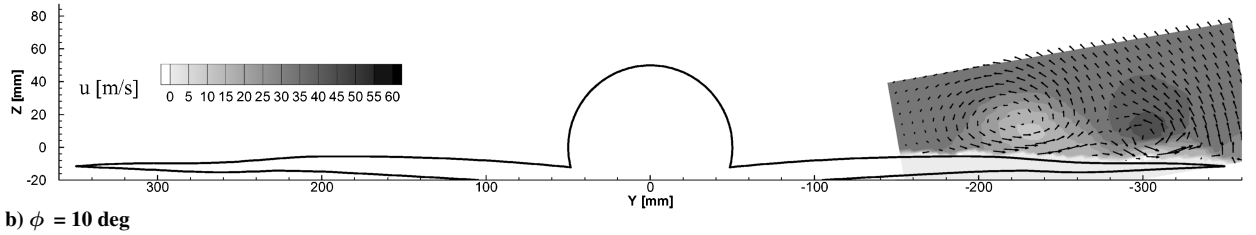

b) ϕ = 10 deg

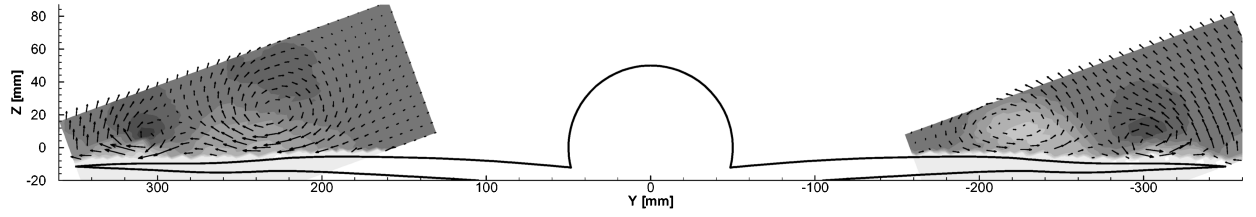

c) ϕ = 20 deg

Fig. 11 Averaged velocity vectors and streamwise velocity contour at different roll angles, $\sigma = 12$ deg and $x/c_r = 0.83$.

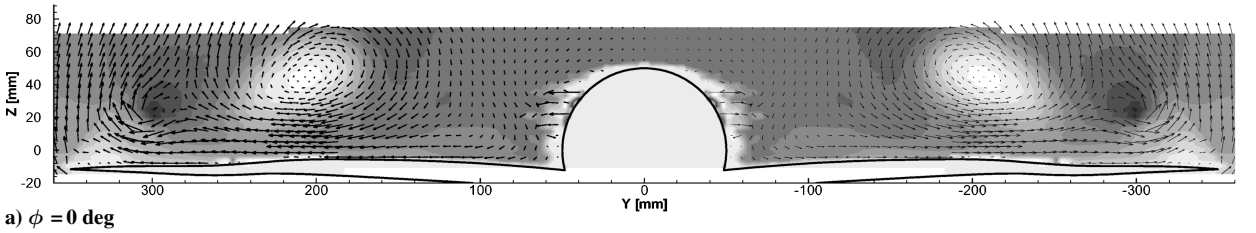

a) ϕ = 0 deg

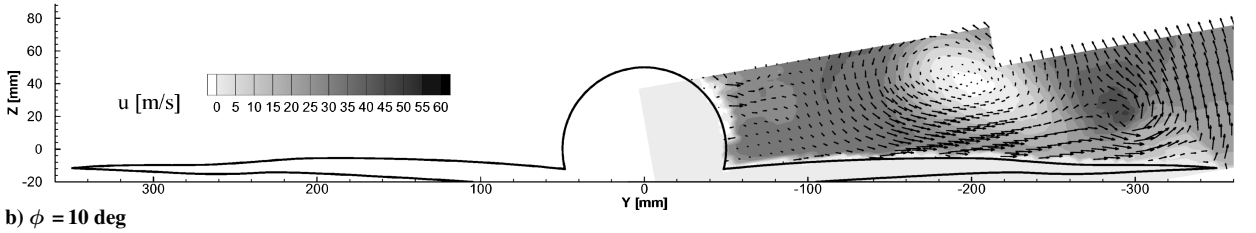

b) ϕ = 10 deg

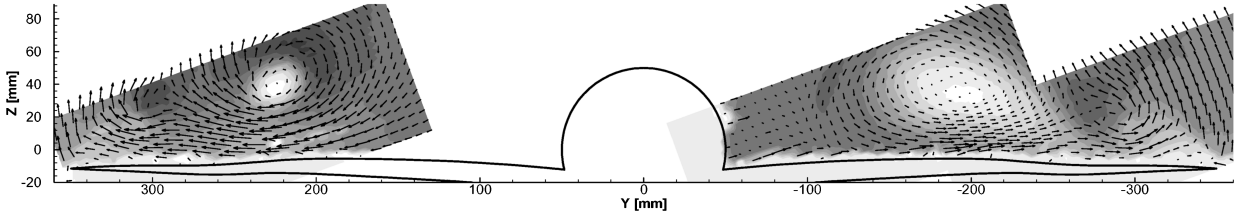

c) ϕ = 20 deg

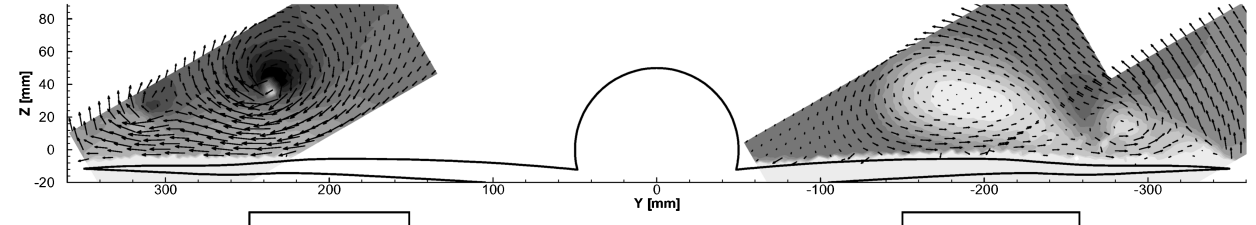

d) ϕ = 30 deg

Fig. 12 Averaged velocity vectors and streamwise velocity contour at different roll angles, $\sigma = 20$ deg and $x/c_r = 0.83$.

Force measurement results in Figs. 4 and 5 indicated that the abrupt increment of the unstable rolling moment is strongly related to the abrupt increment of the nose-down pitching moment. The increment of suction peaks at $x/c_r = 0.83$ on the leeward wing due to the retreat of the vortex breakdown induces the increase in the nose-down pitching moment (where C_m measured about 0.25 c_{mac}), whereas decrement of the suction peaks at $x/c_r = 0.83$ on the windward wing induces the decrease in the nose-down moment. If the effect of the movement of vortex breakdown position on the leeward wing is larger than that on the windward wing, a sudden increment of nose-down pitching moment could occur. Therefore, the occurrence of abrupt changes of rolling moment from a stable to unstable state and also the sudden increment of the nose-down pitching moment can be attributed to the breakdown of the inboard vortex on the leeward wing at $x/c_r = 0.83$ and $\sigma = 20$ deg, as discussed earlier.

V. Conclusions

Wind-tunnel tests were performed to investigate rolling moment characteristics of a cranked arrow wing configuration. Force and surface static pressure measurements were conducted when the model was rolled statically. To understand the behavior of the leading-edge separation vortex, stereoscopic PIV surveys were also performed. The results are summarized as follows.

1) When the roll angle of the model is increased, linearly stable rolling moments act on the model at low incidence angles. On the other hand, drastic changes of rolling moments from a stable to an unstable state are observed at an incidence angle of 20 deg. This change in the rolling moment is strongly related to the abrupt increment of the nose-down pitching moment.

2) Variations in suction peaks in the static pressure distributions at $x/c_r = 0.83$ and $\sigma = 20$ deg contribute to the abrupt increment of the unstable rolling moment. These variations in suction peaks are related to vortex breakdown characteristics. The asymmetry of the chordwise locations of inboard vortex breakdown on the windward and leeward wings produces a drastic change in rolling moments.

Acknowledgments

The authors gratefully acknowledge Shigeya Watanabe, Hiroyuki Kato, and Takuya Hashimoto of Advanced Technology Group, Japan Aerospace Exploration Agency (JAXA) for their contribution of particle image velocimetry survey and data analysis. Toshimi Fujita and Akihito Iwasaki of the Low Speed Wind Tunnel Group, JAXA, aided in wind-tunnel experiments, and their helpful support is also acknowledged.

References

[1]Polhamus, E. C., "Prediction of Vortex Lift Characteristics by a Leading-Edge Suction Analogy," *Journal of Aircraft*, Vol. 8, No. 4, 1971, pp. 193–199.

[2]Erickson, G. E., "Flow Studies of Slender Wing Vortices," AIAA Paper 80-1423, July 1980.

[3]Ericsson, L. E., "The Fluid Mechanics of Slender Wing Rock," *Journal of Aircraft*, Vol. 21, No. 5, 1984, pp. 322–328.

[4]Zohar, Y., and Er-El, J., "Influence of the Aspect Ratio on the Aerodynamics of the Delta Wing at High Angle of Attack," *Journal of Aircraft*, Vol. 25, No. 3, 1988, pp. 200–205.

[5]Katz, J., and Levin, D., "Static Measurement of Slender Delta Wing Rolling Moment Hysteresis," *Journal of Aircraft*, Vol. 28, No. 4, 1991, pp. 282–283.

[6]Sato, J., Fujii, K., Umezawa, D., and Sunada, Y., "Experimental Aerodynamics on Rolling Delta Wing at High Angles of Attack," *Fluid Dynamics of High Angle of Attack*, Spring-Verlag, Berlin, 1992, pp. 425–439.

[7]Visser, K. D., and Nelson, R. C., "Measurement of Circulation and Vorticity in the Leading-Edge Vortex of a Delta Wing," *AIAA Journal*, Vol. 31, No. 1, 1993, pp. 104–111.

[8]Jenkins, J. E., Myatt, J. H., and Hanff, E. S., "Body-Axis Rolling Motion Critical States of a 65-Degree Delta Wing," AIAA Paper 93-0621, Jan. 1993.

[9]Hummel, D., and Srinivasan, P. S., "Vortex Breakdown Effects on the Low-Speed Aerodynamic Characteristics of Slender Delta Wings in Symmetrical Flow," *Journal of Royal Aeronautical Society*, Vol. 71, No. 676, 1967, pp. 319–322.

[10]Wentz, W. H., Jr., and Kohlman, D. L., "Vortex Breakdown on Slender Sharp-Edged Wings," *Journal of Aircraft*, Vol. 8, No. 3, 1971, pp. 156–161.

[11]Terry, T., Malcolm, G. N., and Lewis, L. C., "Experimental Study of Vortex Flows over Delta Wings in Wing Rock Motion," *Journal of Aircraft*, Vol. 29, No. 4, 1992, pp. 598–603.

[12]Kwak, D. Y., "Unsteady Aerodynamic Characteristics on Rolling Delta Wings," *Journal of Japan Society for Aeronautical and Space Sciences*, Vol. 47, No. 543, 1999, pp. 165–173 (in Japanese).

[13]Degani, D., and Zilliac, G. G., "Experimental Study of Nonsteady Asymmetric Flow Around an Ogive–Cylinder at Incidence," *AIAA Journal*, Vol. 28, No. 4, 1990, pp. 642–649.

[14]Brennenstuhl, U., and Hummel, D., "Vortex Formation over Double-Delta Wing," *Proceeding of 13th Congress of the International Council of the Aeronautical Sciences*, International Council of the Aeronautical Sciences, Seattle, WA, 1982, pp. 1133–1146.

[15]Verhaagen, N. G., Jenkins, L. N., Kern, S. B., and Washburn, A. E., "A Study of the Vortex Flow over 76/40-deg Double-Delta Wing," AIAA Paper 95-0650, Jan. 1995.

[16]Yoshida, K., Makino, Y., and Shimbo, Y., "An Experimental Study on Unmanned Scaled Supersonic Experimental Airplane," AIAA Paper 2002-2842, June 2002.

[17]Rinoie, K., Miyata, K., Kwak, D. Y., and Noguchi, M., "Studies on Vortex Flaps with Rounded Leading-Edges for Supersonic Transport Configuration," *Journal of Aircraft*, Vol. 41, No. 4, 2004, pp. 829–838.

[18]Watanabe, S., Kato, H., Kwak, D. Y., Shirotake, M., and Rinoie, K., "Stereo PIV Measurements of Leading-Edge Vortices on a Cranked Arrow Wing," *Measurement Science & Technology*, Vol. 15, No. 6, 2004, pp. 1079–1089.

[19]Verhaagen, N. G., and Naarding, S. H. J., "Experimental and Numerical Investigation of Vortex Flow over a Sideslipping Delta Wing," *Journal of Aircraft*, Vol. 26, No. 11, 1989, pp. 971–978.

[20]Ericsson, L. E., and Hanff, E. S., "Further Analysis of High-Rate Rolling Experiments of a 65-Deg Delta Wing," *Journal of Aircraft*, Vol. 31, No. 6, 1994, pp. 1350–1357.

[21]Jobe, C. E., Hsia, A. H., Jenkins, J. E., and Addington, G. A., "Critical States and Flow Structure on a 65-Deg Delta Wing," *Journal of Aircraft*, Vol. 33, No. 2, 1996, pp. 347–352.

[22]Arena, A. S., and Nelson, R. C., "Unsteady Surface Pressure Measurements on a Slender Delta Wing Undergoing Limit Cycle Wing Rock," AIAA Paper 91-0434, Jan. 1991.

[23]Chaderjian, N. M., "Navier–Stokes Prediction of Large-Amplitude Delta-Wing Roll Oscillations," *Journal of Aircraft*, Vol. 31, No. 6, 1994, pp. 1333–1340.